

Fabrication of a novel PANI/[Co(NH₃)₄(C₃H₄N₂)₂]Cl₃ nanocomposite with enhanced dielectric constant and ac-conductivity

Waseem Naqash¹ · Kowsar Majid¹

Received: 16 April 2017 / Accepted: 2 June 2017 / Published online: 19 June 2017
© Springer Science+Business Media, LLC 2017

Abstract A new polyaniline/[Co(NH₃)₄(C₃H₄N₂)₂]Cl₃ nanocomposite was synthesised by in-situ oxidative polymerisation of aniline monomer in non-aqueous DMSO medium. The nanocomposite was investigated as a suitable material for energy storage and high frequency device applications due to its high value of dielectric constant ($\approx 10^4$) and ac-conductivity ($\approx 10^8$) with a rapid decrease in loss tangent in the high frequency region. The nanocomposite was characterised by techniques like UV–Vis spectroscopy, Fourier transform infrared spectroscopy, X-ray diffraction analysis and field emission scanning electron microscopy (FESEM). The results revealed presence of photoadduct (PA) in PANI@PA nanocomposite with significant interaction between PANI matrix and PA nanoparticles. The PANI@PA nanocomposite exhibit enhanced thermal stability broadening its scope of usability. The better dispersion of PA nanoparticles in the PANI matrix as observed in FESEM, facilitates better charge transport. Dielectric study showed capacitive effect of the nanocomposite at low frequency and a conductivity effect at high frequency. The high value of dielectric constant and ac-conductivity of PANI@PA nanocomposite is attributed to the heterogeneous structure of nanocomposite with enhanced interface, which has a positive effect on the dielectric properties of the material.

1 Introduction

Electrical energy storage plays an important role in electronic devices, stationary power systems, pulse power applications etc. [1, 2]. There is a growing need to develop such dielectric materials which can be used to store large amount of energy in the form of charge separation and then deliver it instantaneously. This has led to the development of polymer nanocomposite materials that combine the processability of the polymers with high dielectric constant of inorganic fillers. These inorganic–organic nanocomposites have been extensively studied in the recent years due to their improved electrical, thermal, structural, optical and magnetic properties [3–8]. In particular, as the size of filler goes to nanometre scale, the properties of polymer-filler interface become more dominant over the bulk properties of the individual constituents [9, 10]. The unique properties of the interface are amplified by the high surface area of the filler. The better dispersion of dielectric filler particles into the polymer matrix consequently favours enhanced charge transport. This results in increasing the effective dielectric constant and the ac-conductivity of these materials for the fabrication of pulse power energy storage systems and in high frequency device applications. Consequently, much research is carried out to develop such type of inorganic fillers which yield enhanced dielectric permittivity without an unacceptably large increase in dielectric loss i.e. energy dissipation. Recently the photoadducts of some of the photochemically active transition metal complexes have been used as new type of fillers [11–13]. The photoadducts are the photosubstituted products obtained by irradiating the aqueous solution mixture of a photochemically active transition metal complex in presence of some other ligand of our choice. The literature reports enhanced dielectric, thermal and photocatalytic properties of some

✉ Kowsar Majid
kowsarmajid@rediffmail.com; kowsar@nitsri.net

¹ Department of Chemistry, National Institute of Technology Srinagar, Hazratbal Srinagar, J&K 190 006, India

polypyrrole and polythiophene nanocomposites using such type of fillers [14, 15]. Therefore, in this direction we have also tried to synthesise the polyaniline nanocomposite in non-aqueous DMSO medium with the photoadduct of hexaminecobalt(III) chloride $[\text{Co}(\text{NH}_3)_6]\text{Cl}_3$ metal complex and imidazole ligand and investigated its structural, optical, thermal and dielectric properties. The PANI synthesised in aqueous medium is difficult to process due to its insolubility in most organic solvents and infusibility [16]. Besides, the synthesised photoadduct being soluble in water is also difficult to get retained in the PANI matrix. These constraints prompted us to choose a non-aqueous DMSO medium as an in-situ solvent for the synthesis of PANI@PA nanocomposite. The hexaminecobalt(III) chloride metal complex is known for its thermal stability and inert nature and possessing photo reactivity, the property which can be utilised for the synthesis of novel coordination complexes with improvised properties. The imidazole ligand is present in many important biological systems and is also involved in some important biological processes. Synthetic imidazoles are present in many antifungal drugs and it has been used extensively as a corrosion inhibitor. There are two nitrogen atoms in imidazole molecule, among which the deprotonated nitrogen atom is the coordinating source with metal ions, while the protonated one is a good hydrogen bonding donor.

2 Materials and methods

2.1 Materials

The following chemicals and reagents were used as starting materials: aniline (Merck), HCl (Molychem), ammonium persulphate (Rankem), DMSO (Fischer Scientific), and imidazole (Sigma Aldrich). Triple distilled water obtained from Borosil mono quartz distillation unit was used throughout the experimental work. All reagents were of analytic grade and used as received.

2.2 $[\text{Co}(\text{NH}_3)_4(\text{C}_3\text{H}_4\text{N}_2)_2]\text{Cl}_3$ photoadduct (PA) synthesis

Aqueous solutions of hexaminecobalt(III) chloride metal complex and imidazole were mixed in a 1:2 molar ratio (0.2 M metal complex and 0.4 M imidazole). The solution mixture was then irradiated in the ligand field region, using Osram photo lamp for half an hour. Colour of the solution mixture changed from orange to deep red. The solution was concentrated on a water bath to obtain solid PA which was subsequently dried in a vacuum desiccator.

The as prepared PA was subjected to high energy milling using planetary PM 100 high energy ball mill, to

obtain a nano powder. Ten balls of Zirconium metal having 10 mm diameter and 0.85 g weight were used to grind the sample maintaining a weight ratio of 1:5 between the sample and the balls. The sample was milled for 12 h at a fixed rotational speed of 450 rpm with fixed time intervals of 5 min. After each interval, the sample was subjected to reverse rotation to ensure successful nano size reduction. The synthesised PA nano powder was subjected to various spectroscopic and surface characterisations to confirm its successful synthesis and nano dimensions.

2.3 PANI/photoadduct nanocomposite (PANI@PA) synthesis

1.0 g of PA nano particles were dispersed into a precooled solution of 1 ml distilled aniline in 10 ml of 5 N HCl in DMSO via sonication for 10 min to obtain a uniform suspension. 1.2 g of ammonium persulphate dissolved in 10 ml of DMSO was slowly added into this suspension with continuous stirring for a period of 30 min. The mixture was then allowed to polymerize at 10 °C for 12–24 h with occasional stirring. The resultant PANI@PA nanocomposite was filtered under pressure and washed repeatedly with a mixture of acetone and HCl. Finally, the filtered nanocomposite was dried at 30 °C under vacuum for 24 h. The dried material was grinded to a dark fine fluffy powder. The percentage yield of the product obtained was about 68%.

2.4 Characterisations

The synthesis of samples and their optical property measurement were estimated by UV–VIS double beam spectrophotometer (PG Instruments T80) in the wavelength range of 200–800 nm at a scan rate of 100 nm/min. The structural characteristics of the samples were measured by Fourier transform infrared (Perkin Elmer RX-1 FTIR spectrophotometer) and X-ray diffraction (XPRTPRO PW-3050 base diffractometer) spectroscopy. The surface morphology of the samples was observed by field emission scanning electron microscope (FESEM, Hitachi S-4700). Thermal analysis of the samples was done on PerkinElmer thermal analyser from ambient to 700 °C temperature, at a heating rate of 20 °C/min under nitrogen atmosphere. Dielectric studies have been carried out on Wayne Kerr 6440B, Precision impedance analyser in the frequency range of 20 Hz to 3 MHz at room temperature. For this purpose the powdered sample was compressed into a circular pellet on a hydraulic press by applying a pressure of 10 tons. The thickness and diameter of the pellet were 1.145 and 6.677 mm respectively and the pellet was coated on both sides with graphite prior to measurement for making a parallel plate capacitor arrangement.

3 Results and discussion

3.1 Elemental analysis

The CHN elemental analysis observed for photo derivative product (PA) was found to be: C, 16%; H, 6%; and N, 24%. On this basis the proposed empirical formula of PA was given as: $[\text{Co}(\text{NH}_3)_4(\text{C}_3\text{H}_4\text{N}_2)_2]\text{Cl}_3$, for which the percentage of C, H and N was calculated as 15.48, 4.30 and 24.08% respectively.

3.2 Structural characteristics

The structural properties of the as synthesised PA and PANI@PA were studied by employing FTIR, XRD and FESEM techniques.

3.3 FTIR spectral characterisation

FTIR spectroscopy was used to ascertain the chemical structure and possible interactions between PA and PANI in PANI@PA. Figure 1 shows the FTIR spectra of PA, pure PANI and PANI@PA. The FTIR spectra of PA show peaks corresponding to hexamine metal complex as well as that of incorporating imidazole ligand. The characteristic peaks in the FTIR spectra of PA at 3133, 1600, 1325 and 830 cm^{-1} correspond to stretching, degeneration deformation, symmetric deformation and rocking vibration of complexed (NH_3) molecule respectively. In the IR spectrum of PA, the peaks at (1600, 1489, 1440 cm^{-1}), 1254 cm^{-1} , (1061, 930 cm^{-1}), (751 and 656 cm^{-1}) are attributed to the characteristic peaks of photosubstituted imidazole ligand thereby proving successful

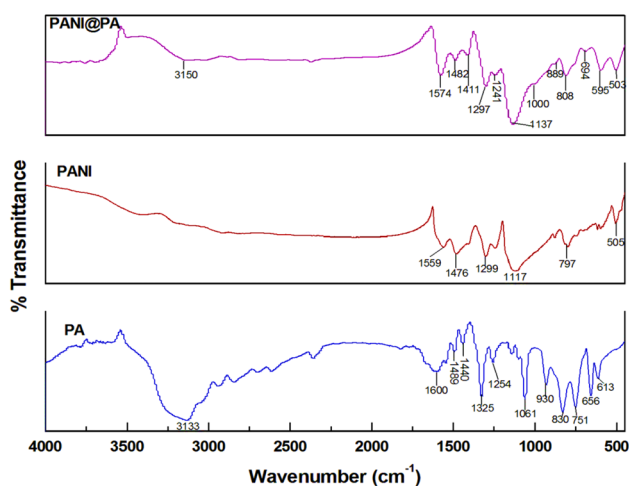


Fig. 1 FTIR spectra of PA, PANI and PANI@PA nanocomposite

photoadduct synthesis. These peaks are credited to C=C and C=N stretching of aromatic ring of imidazole, C–H in plane bending and C–H out of plane bending vibrations respectively. The characteristic peaks in the spectra of pure PANI positioned at 1559, 1476, 1299, 1117, and 797 cm^{-1} are attributed to C–C stretching mode of quinoid ring, C–C bond stretching of benzenoid ring, C–N single bond vibrations, C–H in plane bending and C–H out of plane deformation respectively. The FTIR spectrum of PANI@PA exhibited the homology to pure PANI but with some deviations in peak positions indicating some interactions between PA and PANI backbone chains. All the characteristic peaks of PANI described above appear in PANI@PA but with some deviations and are positioned at 1574, 1482, 1297, 1137 and 808 cm^{-1} in the nanocomposite. Furthermore, the presence of the additional bands around 3150, 1411, 1241, 1000 and 889 cm^{-1} are the characteristic peaks of PA which are observed in nanocomposite with some deviations, thereby revealing the presence of PA in the PANI matrix.

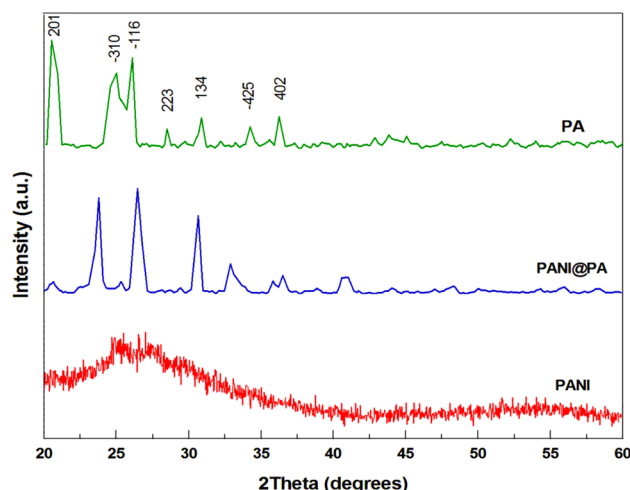


Fig. 2 XRD patterns of PANI, PANI@PA nanocomposite and PA

Table 1 Evaluated parameters from XRD data of PA

<i>h</i>	<i>k</i>	<i>l</i>	$2\theta^\circ$	<i>d</i> (Å)	FWHM
2	0	1	20.569	4.3145	1.3190
$\bar{3}$	1	0	25.002	3.5586	2.5340
$\bar{1}$	1	6	26.053	3.4174	2.5340
2	2	4	28.490	3.1304	0.8920
1	3	4	30.886	2.8917	0.6720
$\bar{4}$	2	5	34.248	2.6163	1.0960
4	0	2	36.318	2.0615	1.0970

3.4 X-ray diffraction analysis

Figure 2 shows the XRD spectra of all samples i.e. pure PANI, PA and PANI@PA. The related data is given in Table 1. The XRD spectrum of PANI does not show any sharp peak but rather a broad hump ranging from 20° to 30° suggesting an amorphous nature of PANI. This is in consistent with the results obtained by other research groups [17–19]. The PANI@PA shows crystalline peaks due to the presence of PA in the nanocomposite. The broad diffused peak of PANI disappears in nanocomposite as the PA nanoparticles interfere with PANI chains. The XRD spectrum of PA shows sharp peaks characteristic of a crystalline material around 2 θ , 20.57°, 25.00°, 26.05°, 28.49°, 30.89°, 34.25° and 36.25°. The crystalline peaks of PA are a result of reflection from the following reflection planes: (201), ($\bar{3}$ 10), ($\bar{1}$ 16), (223), (134), ($\bar{4}$ 25) and (402). These planes indicate the presence of a monoclinic structure of PA with lattice type 'C' (space group C_2/m (12)). Almost all these peaks appear in nanocomposite with a shift of $\pm 1.0^\circ$, which shows a successful interaction between PA and PANI in nanocomposite. The average crystallite size of PA and PANI@PA was calculated from line broadening using the Debye-Scherrer's formulae:

$$D = 0.9\lambda / \beta \cos\theta$$

where, λ is the X-ray wavelength, β is the line broadening at the full-width at half maximum of most intense peak (FWHM) and θ is the corresponding Bragg's angle [20–22]. The calculated crystallite size of PA and PANI@PA were found to be 25.97 and 28.77 nm respectively. Lattice parameters (a , b , c and β) were calculated for the monoclinic structure of PA and were found to be 12.10, 12.75, 21.44 Å and 113.5° respectively. The values are in good agreement with the JCPDS- International centre for diffraction data, file No. 70-0787.

3.5 FE-SEM characterisation

The microstructure of the as synthesised PA and PANI@PA nanocomposite were analysed by field emission scanning electron microscopy and is shown in Fig. 3. The scanning electron micrograph of PA reveals the presence of irregular photoadduct particles with compact structure as compared to nanocomposite, which displays rough mixed morphology in which PA nanoparticles are more or less uniformly covered by PANI material. The PANI chains enclose the PA nanoparticles and the nanocomposite grows as multiparticles as reported in the literature [23–26]. The SEM image was imported into the image J software and the average size distribution of the particles was determined and is shown in Fig. 3c.

3.6 Optical properties characterisation

3.6.1 UV-visible analysis

In order to confirm the expulsion of ammonia ligand from $[\text{Co}(\text{NH}_3)_6]\text{Cl}_3$ and its subsequent substitution by imidazole, UV-Vis spectra in the wavelength range of 200–800 nm was observed for hexaminecobalt(III) chloride metal complex with imidazole ligand before and after irradiation and is shown in Fig. 4. Before irradiation, the hexamine metal complex show three bands in the UV-Vis spectrum. The intense band which appears at 235 nm is attributed to spin allowed LMCT transition whereas the two peaks at 335 and 475 nm correspond to ligand field bands. However, after irradiation the ligand field band at 335 nm is shifted to 325 nm as a shoulder and the LMCT band at 235 nm is shifted to 240 nm. Thus, a spectral change has occurred which indicates a change in the ligand field environment around the Co(III) metal ion by ligand substitution process. This confirms the successful photosubstitution by the imidazole ligand.

3.6.2 UV-Visible spectroscopy of PANI and PANI@PA nanocomposite

The UV-Vis absorption method was carried out for spectroscopic investigation of the polymer and polymer nanocomposite. UV-Vis absorption spectra of PANI and PANI@PA were recorded in the wavelength range of 200–800 nm using *N*-methyl-2-pyrrolidone (NMP) as a solvent and are shown in Fig. 5. The UV-Vis spectrum of PANI shows a peak corresponding to $\pi \rightarrow \pi^*$ transition within the benzenoid segment at 320 nm and a major peak at 440 nm which is attributed to polaron $\rightarrow \pi^*$ transition. Moreover, a hump called as broad free carrier band around 565 nm is also observed, which along with 440 nm peak is related to the doping level in PANI [6, 7]. In case of PANI@PA nanocomposite both the 440 nm peak and the hump at 565 nm are shifted to 415 and 550 nm respectively. This shift in the absorption bands reflects the modification of PANI by PA nanoparticles. Besides, the presence of a shoulder at 265 nm in the spectrum of nanocomposite is because of PA which shows its presence in case of pure PA at 240 nm. The presence of this shoulder with a shift in position confirms the presence of PA nanoparticles in the nanocomposite and their interaction with PANI. This is also supported by FTIR characterization of the samples.

The energy band gap of PA, PANI and PANI@PA was also calculated from their absorption spectra using Tauc relation [27]:

$$\alpha h\nu = A(h\nu - E_g)^n$$

where, α is the absorption coefficient, A is a constant, $h\nu$ is the photonic energy, E_g is the energy band gap and n is an

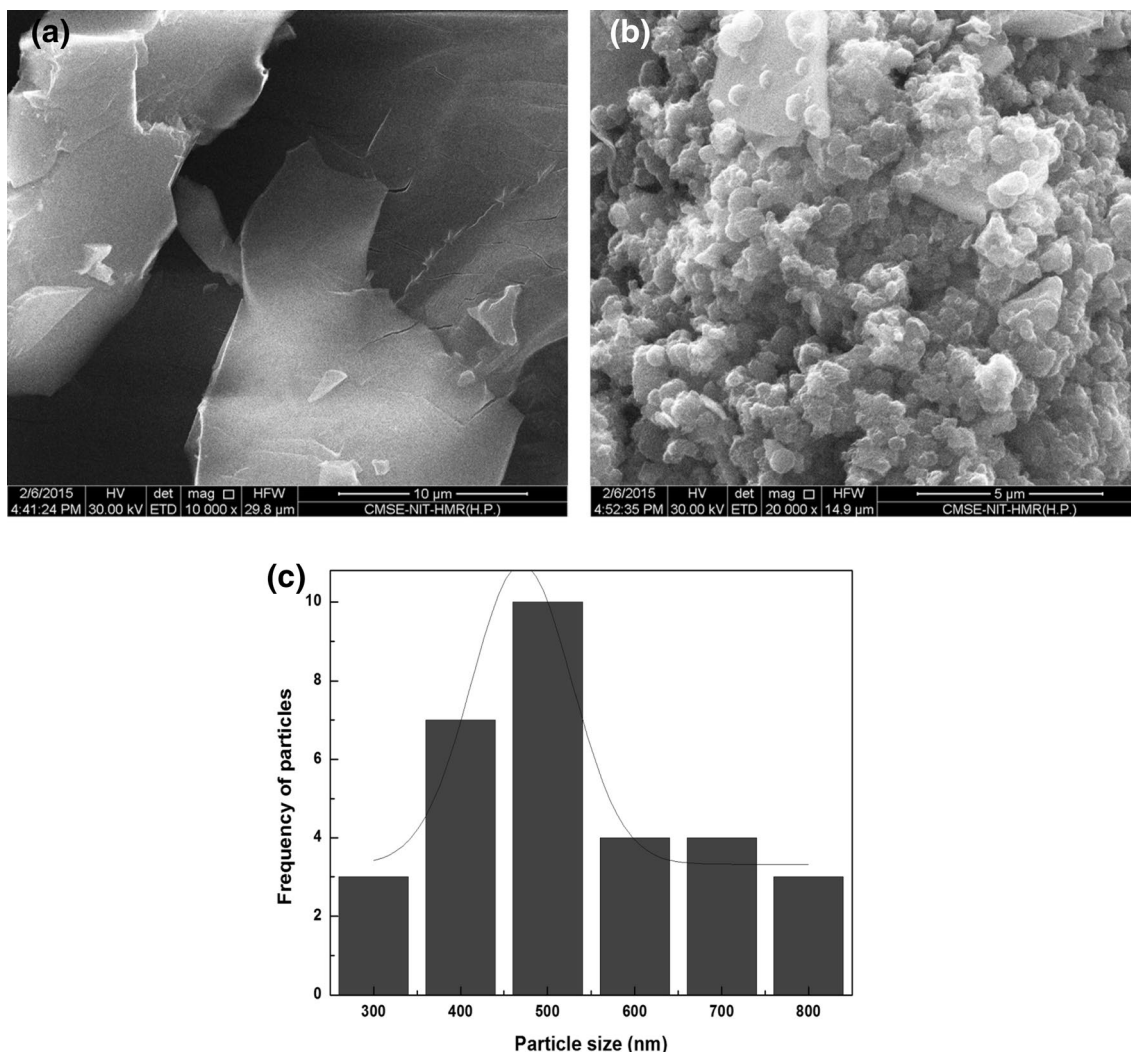


Fig. 3 High resolution FESEM images of **a** PA **b** PANI@PA nanocomposite and **c** histogram of particle size distribution

index describing the electronic transition process, which is related to density of states. It possesses discrete values of 1/2, 3/2, 2 and 3 for direct allowed, direct forbidden, indirect allowed and indirect forbidden transition respectively [27]. The intercept of extrapolated linear region of plot $(\alpha h\nu)^{1/n}$ versus $h\nu$ on x-axis gives the value of the optical band gap E_g as shown in Fig. 6 and the value of n determines the type of transition. As such, the band gap for PA, PANI and PANI@PA were found to be 3.00, 1.55 and 1.70 eV respectively.

3.7 Thermal properties characterisation

3.7.1 Thermal gravimetric analysis (TGA)

TGA curves of PA and PANI@PA are shown in Fig. 7. It is observed that PA shows weight loss in three stages of decomposition. The first transition in PA commences from

100 °C with a weight loss of 38% (against the calculated weight loss of 36.85%) which can be attributed to the loss of C, H, N moieties of two imidazole ligand molecules and ends at 230 °C. The second stage of decomposition starts from 230 °C up to 350 °C involving two consecutive weight loss of 19% (against the calculated loss of 18.97%) and 11% (against the calculated loss of 9.89%) corresponding to the loss of three counter Cl^- ions of PA as Cl_2 molecule and a molecule of HCl. Third transition in PA starts from 350 °C and ends at 750 °C with a weight loss of 17% (against the calculated loss of 18.42) due to the loss of four ammine ligands; thereafter the thermogram runs parallel to temperature axis with approximately 15% of residue left. The TGA curve of pure PANI as reported by many researchers [28–31] shows an early weight loss of about 5% due to the loss of moisture within the layers. The curve then shows stability up to 250–350 °C, wherefrom it undergoes a fast decomposition of about 80–95%, which lasts up

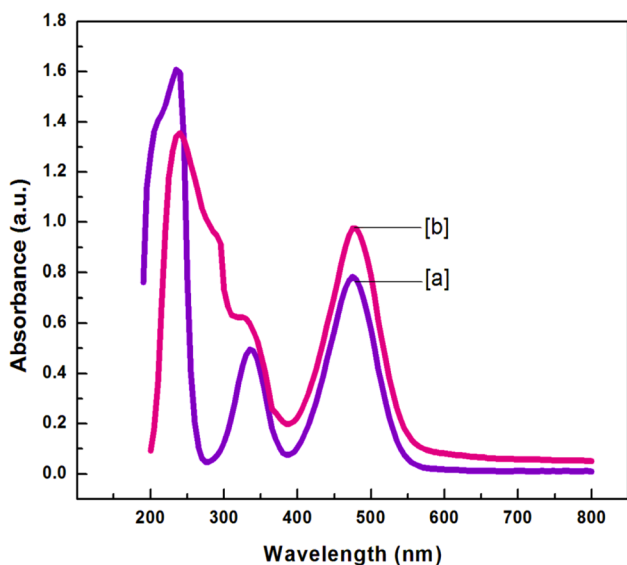


Fig. 4 UV–Vis spectra of $[\text{Co}(\text{NH}_3)_6]\text{Cl}_3/\text{imidazole}$ solution mixture [a] before [b] after irradiation

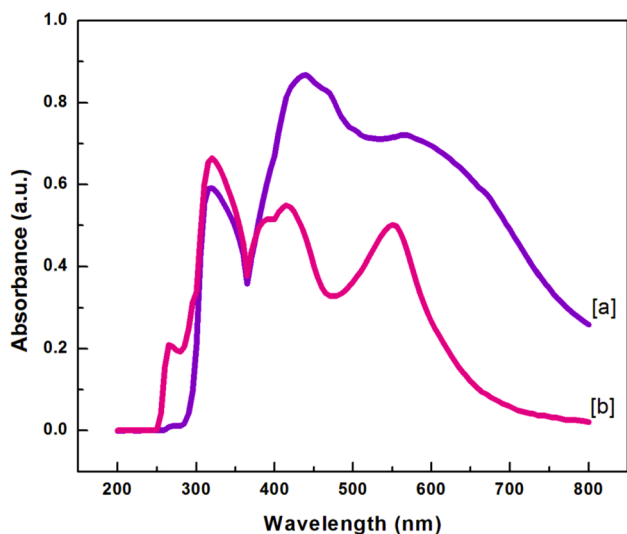


Fig. 5 UV–Vis absorption spectra of [a] PANI and [b] PANI@PA nanocomposite

to 600–700 °C, attributing to the thermal degradation of polymer chains. The residue left in pure PANI as reported in the literature varies from 0 to 15% at 700 °C. The thermal decomposition of PANI@PA is shown in Fig. 7b. The first transition in case of PANI@PA nanocomposite commences at around 215 °C. The transition is a sharp one with a total weight loss of about 21% due to the loss of moisture, unreacted HCl and low molecular weight polymer chains. The second transition starts from 216 °C and ends at 310 °C with a weight loss of 42% corresponding to the degradation of polymer chains and the loss of PA from PANI@

PA nanocomposite. From 310 °C onwards the thermogram runs almost parallel to temperature axis depicting enhanced thermal stability of nanocomposite over PANI. The residue left at 700 °C is around 30% which is higher than that of both PA and pure PANI. The higher thermal stability of these nanocomposite materials envisages them as good candidates for melt blending with conventional thermoplastics like polyethylene, polystyrene, polypropylene etc [32].

3.8 Electrical properties characterisation

3.8.1 Dielectric characteristic measurements

The various dielectric parameters have been calculated in the frequency range of 20 Hz to 3 MHz using the following equations:

$$\epsilon' = C_p d / \epsilon_o A$$

$$\epsilon'' = \epsilon' \tan \delta$$

$$\tan \delta = \epsilon'' / \epsilon'$$

$$\sigma_{ac} = 2\pi f \epsilon''$$

where, C_p is the capacitance measured in pF, ϵ_o is the permittivity of free space (8.854×10^{-12} F/m), A and d the area and thickness of the sample respectively. ϵ' and ϵ'' are, respectively, the real and imaginary parts of the complex dielectric constant, $\epsilon(f) = \epsilon'(f) - i\epsilon''(f)$, $\tan \delta$, the dielectric loss with δ being phase angle and σ_{ac} the ac-conductivity.

The variation of real and imaginary part of dielectric constant of PANI@PA nanocomposite, with the frequency (20 Hz $< f <$ 3 MHz) at room temperature is shown in Fig. 8a, b. It is apparent from the figure that both ϵ' and ϵ'' shows normal dispersion behaviour as per Maxwell–Wagner model [36]. The real dielectric constant has a value of 5.8×10^4 at 25 Hz which reduces to 1.4×10^4 at 10^2 Hz while as the imaginary part of dielectric constant has a value of 3.1×10^5 at 25 Hz which reduces to 8.5×10^4 at 10^2 Hz. Thus the decrease is rapid (more in ϵ'' than ϵ') in the low frequency region, while it approaches almost frequency independent behaviour in the high frequency region. It is due to the reason, that upon increase in the frequency of applied field, the dipoles present in the system cannot reorient themselves as quickly as the changing field thereby reducing the dielectric constant [37]. The imaginary part of dielectric constant ϵ'' is called the dielectric loss, as it gives the dissipation of applied field energy into the sample due to charge migration i.e. conduction or conversion into thermal energy. The decrease in the value of ϵ'' with frequency can be attributed to the predominance of dc-conduction in the material at low frequency. This is justified from the plot of $\ln \epsilon''$ versus $\ln \omega$ (where, ω is the angular frequency)

Fig. 6 Tauc plots depicting band gap of PA, PANI and PANI@PA nanocomposite

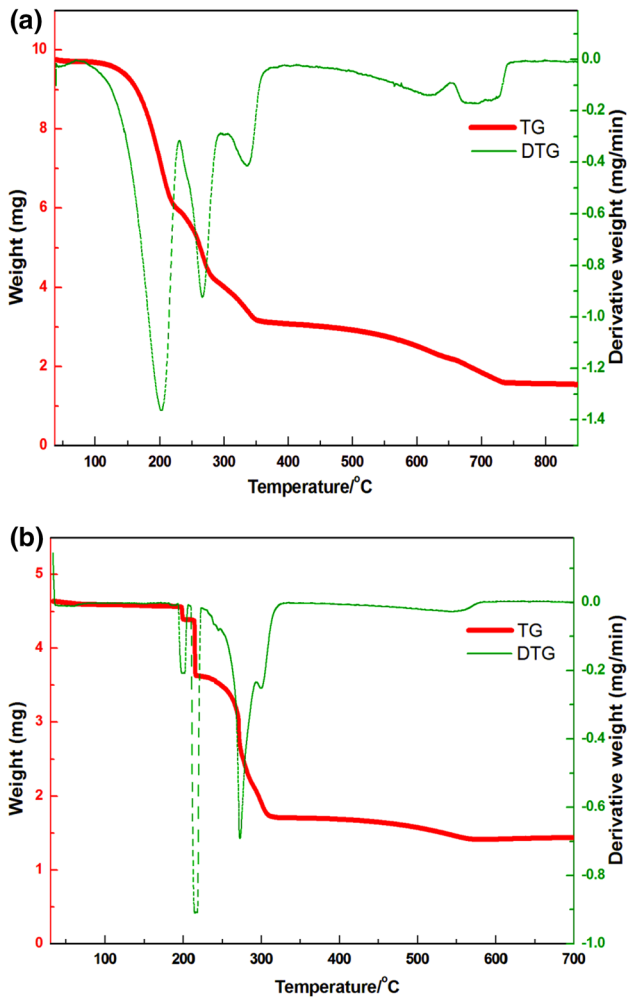
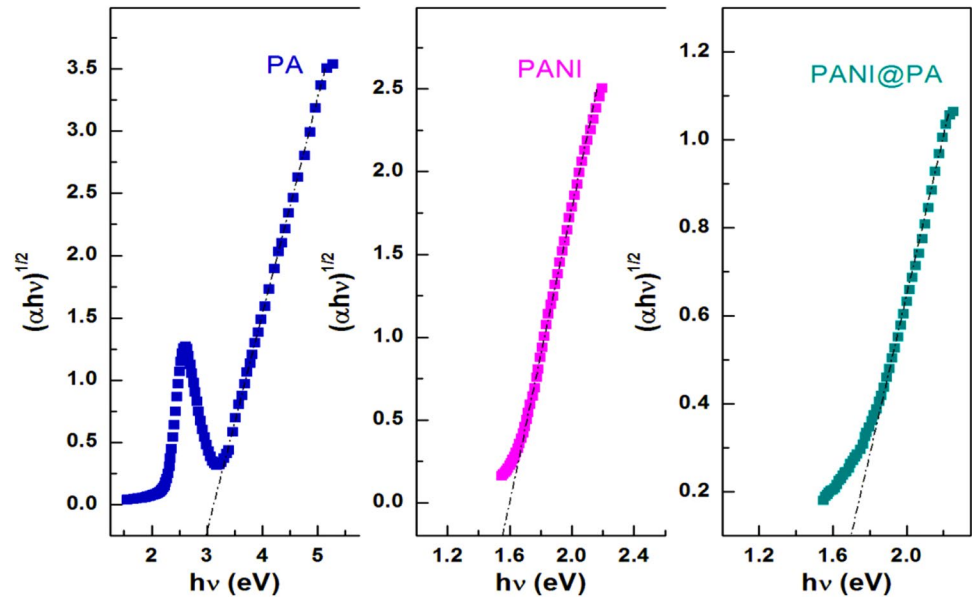


Fig. 7 TG/DTG trace of **a** PA and **b** PANI@PA nanocomposite

which gives a straight line as per the relation: $\epsilon'' = A\omega^m$, where A is a constant.

The slope of fitted curve was found to be -0.90 , (Fig. 8e) which is very close to -1.0 indicating dc-conduction dominant in the material at low frequency. The high value of dielectric constant of the nanocomposite makes it suitable as a capacitor for energy storage applications.

Figure 8c shows the variation of loss tangent ($\tan \delta$) with the frequency of applied field. The dielectric loss gives the loss of energy from applied field into the sample. The $\tan \delta$ is observed to show resonating behaviour around 3020 Hz when the jumping or hopping frequency of charge carriers becomes approximately equal to the frequency of applied field [35]. Thus a relaxation peak appears in $\tan \delta$ followed by subsequent rapid decrease in the high frequency region. However, no such relaxation peak was observed in the spectra of ϵ'' which may be due to the masking of relaxation process by electrical conduction mechanism [36].

The variation of ac-conductivity with the frequency of applied field is shown in Fig. 8d. It reveals that below 10^4 Hz, it is almost independent of applied field frequency indicating dominance of dc-conductivity in the material at low frequency. At high frequency region the conductivity shows an exponential increase with the frequency of applied ac-field indicating frequency dependent ac-conduction. In this region the transport is dominated by hopping mechanism. Consequently, the increase in field frequency enhances the hopping frequency of charge carriers resulting in an increase in the conductivity [37]. The frequency dependence of the ac conductivity is considered to be a result of interface charge polarization (Maxwell–Wagner–Sillars effect) and intrinsic electric dipole polarization [38–40]. This phenomenon appears in

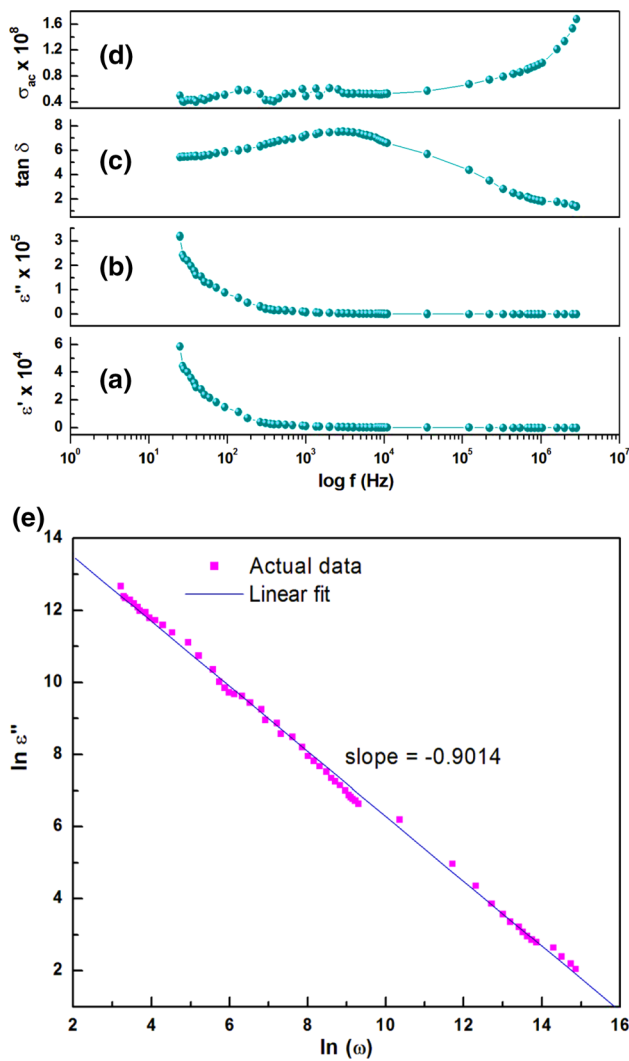


Fig. 8 variation of **a** real **b** imaginary part of dielectric constant **c** loss tangent **d** ac-conductivity of PANI@PA nanocomposite as a function of frequency **e** plot of $\ln \epsilon''$ vs. $\ln(\omega)$

heterogeneous system like PANI-PA nanocomposites due to the accumulation of mobile charges at the interfaces. The total conductivity of a dielectric material is the summation of band and hopping process [41] as shown in the relation:

$$\sigma_{total} = \sigma_o(T) + \sigma(\omega, T)$$

where, the first term in the equation is frequency independent dc-conductivity, the second term is the frequency dependent ac-conductivity which is related to dielectric relaxation caused by the localized charge carriers. The ac-conductivity of the PANI@PA nanocomposite is very high of the order of 10^8 which is explained from the effective dispersion of PA nanoparticles in the PANI matrix (as observed in SEM image), which favours better charge

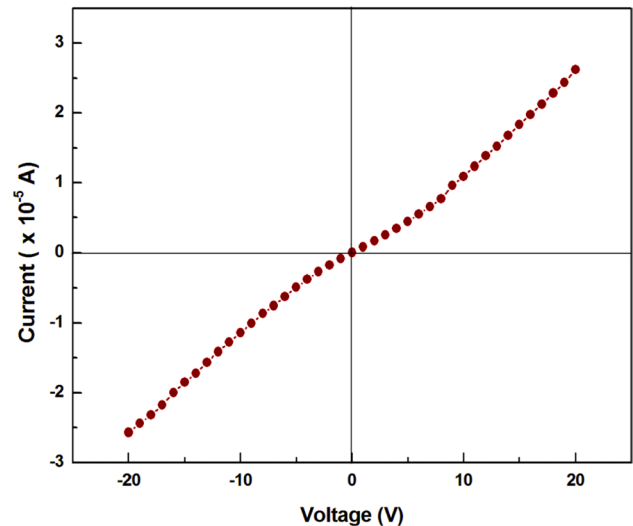


Fig. 9 I–V characteristic of PANI@PA nanocomposite

transport. This high value of ac-conductivity and rapid dielectric loss of the material in the high frequency region makes the nanocomposite suitable in high frequency device applications.

3.9 Current–voltage (I–V) characteristics

Figure 9 shows the non-linear I–V curve of PANI@PA nanocomposite which is symmetrical in both forward and reverse bias and showing non-ohmic variation. The non-linear variation of current with the applied voltage is explained by the fact that the current is carried not only by free charge carriers i.e. electrons and holes as in case of conventional semiconductors, but also by formation of polarons and bipolarons. As the applied voltage is increased, more polarons and bipolarons are formed resulting in higher values of current. The conductivity of the nanocomposite (σ_{dc}) has been obtained using the relation:

$$\sigma_{dc} = I/V$$

where the terms have their usual meanings. The observed conductivity of the material at 5 V was found to be 0.01 mS/m.

4 Conclusion

Synthesis of PA has been carried out through photosubstitution route, which was subjected to nano size reduction prior to incorporation into the PANI matrix. The empirical formula of PA was found to be $[\text{Co}(\text{NH}_3)_4(\text{C}_3\text{H}_4\text{N}_2)_2]$

Cl₃ from elemental analysis. FTIR, XRD, FESEM and UV–Visible analysis proved the successful synthesis of PA and its nanocomposite. FESEM showed better dispersion of PA nanoparticles in the PANI matrix which facilitated better electrical contact between them. Enhanced thermal stability of PANI@PA nanocomposite as observed from TG/DTG envisages its use for melt blending with conventional thermoplastics and in high temperature applications. Dielectric studies revealed a capacitive effect of the nanocomposite at low frequency and a conductivity effect at high frequency, making the material suitable for electrical energy storage and high frequency device applications.

References

- H. Nalwa, *Handbook of Low and High Dielectric Constant Materials and Their Applications*. (Academic Press, London, 1999)
- T. Osaka, M. Datta, *Energy Storage Systems for Electronics*. (Gordon and Breach, Amsterdam, 2001)
- Y. Ma, N. Li, C. Yang, X. Yang, *Colloids Surf. A* **269**, 1(2003)
- T. Machappa, M.V.N. Ambikka Prasad, *Bull. Mater. Sci.* **35**, 1 (2012)
- N. Parvatikar, S. Jain, S. Khasim *Sens. Actuators B* **114**, 2(2006)
- I. Sedenkova, M. Trchova, J. Stejskal, *Polym. Degrad. Stab* **93**, 12 (2008)
- J. Alam, U. Riaz, S.M. Ashraf, S. Ahmad, *J. Coat. Technol. Res* **5**, 1 (2008)
- K. Majid, R. Tabassum, A. F. Shah, S. Ahmad, M. L. Singla, *J. Mater. Sci.* **20**, 958 (2009)
- T.J. Lewis, *IEEE Trans. Dielectr. Electr. Insul.* **11**, 5 (2004)
- T.J. Lewis, *J. Phys. D* **38**, 2 (2005)
- M. H. Najar, K. Majid, *J. Mater. Sci.* **24**, 11 (2013)
- S. K. Moosvi, K. Majid, *J. Mater. Sci.* **27**, 7 (2016)
- M.H. Najar, K. Majid, *J. Mater. Sci.* **26**, 9 (2015)
- M.H. Najar, K. Majid, *RSC. Adv.* **5**, 07209–107221 (2015)
- S.K. Moosvi, K. Majid, T. Ara, *J. Appl. Polym. Sci.* **27**, 7 (2016)
- P. Ghosh, S. K. Siddhanta, S. R. Haque, A. Chakarpati, *Syn. Met.* **123**, 1 (2001)
- J. Jiang, L. Li, M. Zhu, *React. Funct. Polym* **68**, 1 (2008)
- J. Jiang, L. Li, F. Xu, *J. Phys. Chem. Solids* **68**, 9 (2007)
- H. Guo, H. Zhu, H. Lin, J. Zhang, *Mater. Lett.* **62**, 14 (2008)
- V. Eskizeybek, F. Sari, H. Gulce, A. Gulce, A. Avci, *Appl. Catal. B* **119**, 197–206 (2012)
- S. Min, F. Wang, Y. Han, *J. Mater. Sci.* **42**, 24 (2007)
- M.A. Salem, A.F. Al-Ghonemiy, A.B. Zaki, *Appl. Catal. B* **9**, 1 (2009)
- J. Xu, W. Liu, H. Li, *Mater. Sci. Eng. C* **25**, 4 (2005)
- A. Guinier, *X-ray Diffraction in Crystals, Imperfect Crystals, and Amorphous Bodies*, (W. H. Freeman, San Francisco, 1963)
- S.E. Jacobo, J.C. Apesteguy, R.L. Anton, N.N. Schegoleva, G.V. Kurl'yanskaya, *Eur. Polym. J.* **43**, 4 (2007)
- M. Wan, J. Fan, *Polym. Sci. A* **36**, 15 (1998)
- F.A. Mir, S. Rehman, K. Asokan, S.H. Khan, G.M. Bhat, *J. Mater. Sci.* **25**, 1258 (2014)
- M.S. Rather, K. Majid, R.K. Wanchoo, M.L. Singla, *Synth. Met.* **179**, 60–66 (2013)
- F. A. Rafiqiand K. Majid, *RSC Adv.* **6**, 26 (2016)
- A.H. Elsayed, M.S. MohyEldin, A.M. Elsyed, A. H. Abo Elazm, E.M. Younes, H.A. Motaweh, *Int. J. Electrochem. Sci.* **6**, 206–221 (2011)
- Y.N. Qi, F. Xu, L.X. Sun, *J. Therm. Anal. Calorim.* **94**, 1 (2008)
- H. Bhandari, S.A. Kumar, S.K. Dhawan, *Conducting Polymer Nanocomposites for Anticorrosive and Antistatic Applications*, vol. 13 (INTECH Open Access Publisher, Rijeka, 2012)
- K.W. Wagner, *Ann. Phys* **345**, 5 (1913)
- M. Faisal, S. Khasim, *Bull. Korean Chem. Soc.* **34**, 1 (2013)
- M.A. Dar, K.M. Batoo, V. Verma, W.A. Siddiqui, R.K. Kotnala, *J. Alloys Compd.* **493**, 1 (2010)
- M.H. Lakhdar, B. Ouni, M. Amlouk, *Mat. Sci. Semicond. Process.* **19**, 32–39 (2014)
- M.A. Dar, V. Verma, S.P. Gairola, W.A. Siddiqui, R.K. Singh, R.K. Kotnala, *Appl. Surf. Sci.* **258**, 14 (2012)
- G.M. Tsangaris, G.C. Psarras, *J. Mater. Sci.* **34**, 9 (1999)
- G.C. Psarras, E. Manolakaki, G.M. Tsangaris, *Composites A* **33**, 3 (2002)
- G. Perrier, A. Bergeret, *J. Polym. Sci. B* **35**, 9 (1997)
- P. Dutta, S. Biswas, M. Ghosh, *Synth. Met.* **122**, 2 (2001)